Observations of pores and surrounding regions with CO 4.66 μm lines by BBSO/CYRA

Yongliang Song[1], Xianyong Bai[1,2], Xu Yang[3,4], Wenda Cao[3,4], Han Uitenbroek[5], Yuanyong Deng[1,2], Xin Li[1], Xiao Yang[1], and Mei Zhang[1,2]

[1] Key Laboratory of Solar Activity, National Astronomical Observatories, Chinese Academy of Sciences, Beijing 100101, China
e-mail: ylsong@nao.cas.cn; xybai@nao.cas.cn
[2] School of Astronomy and Space Science, University of Chinese Academy of Sciences, Beijing 100049, China
[3] Big Bear Solar Observatory, New Jersey Institute of Technology, Big Bear City, CA 92314-9672, USA
e-mail: wenda.cao@njit.edu
[4] Center for Solar-Terrestrial Research, New Jersey Institute of Technology, 323 Martin Luther King Boulevard, Newark, NJ 07102, USA
[5] National Solar Observatory, University of Colorado Boulder, 3665 Discovery Drive, Boulder, CO 80303, USA

November 15, 2022

ABSTRACT

Context. Solar observations of carbon monoxide (CO) indicate the existence of lower-temperature gas in the lower solar chromosphere. We present an observation of pores, and quiet-Sun, and network magnetic field regions with CO 4.66 μm lines by the Cryogenic Infrared Spectrograph (CYRA) at *Big Bear Solar Observatory*.
Aims. We used the strong CO lines at around 4.66 μm to understand the properties of the thermal structures of lower solar atmosphere in different solar features with various magnetic field strengths.
Methods. Different observations with different instruments were included: CO 4.66 μm imaging spectroscopy by CYRA, Atmospheric Imaging Assembly (AIA) 1700 Å images, Helioseismic and Magnetic Imager (HMI) continuum images, line-of-sight (LOS) magnetograms, and vector magnetograms. The data from 3D radiation magnetohydrodynamic (MHD) simulation with the *Bifrost* code are also employed for the first time to be compared with the observation. We used the Rybicki-Hummer (RH) code to synthesize the CO line profiles in the network regions.
Results. The CO 3-2 R14 line center intensity changes to be either enhanced or diminished with increasing magnetic field strength, which should be caused by different heating effects in magnetic flux tubes with different sizes. We find several "cold bubbles" in the CO 3-2 R14 line center intensity images, which can be classified into two types. One type is located in the quiet-Sun regions without magnetic fields. The other type, which has rarely been reported in the past, is near or surrounded by magnetic fields. Notably, some are located at the edge of the magnetic network. The two kinds of cold bubbles and the relationship between cold bubble intensities and network magnetic field strength are both reproduced by the 3D MHD simulation with the *Bifrost* and RH codes. The simulation also shows that there is a cold plasma blob near the network magnetic fields, causing the observed cold bubbles seen in the CO 3-2 R14 line center image.
Conclusions. Our observation and simulation illustrate that the magnetic field plays a vital role in the generation of some CO cold bubbles.

Key words. Sun:Magnetic fields—Sun:Atmosphere—Sun:Infrared—Radiative Transfer—Molecular spectroscopy

1. Introduction

The fundamental absorption lines of carbon monoxide (CO) at around 4.66 μm have been observed since the 1970s (e.g., Noyes & Hall 1972; Ayres 1981; Ayres et al. 1986; Farmer & Norton 1989; Solanki et al. 1994; Uitenbroek et al. 1994). The discovery of these strong absorption lines indicates the existence of a large amount of cool gas with a temperature that can be as low as 3700 K in the solar atmosphere (e.g., Noyes & Hall 1972; Ayres & Testerman 1981; Ayres & Brault 1990). From observations and simulation models, it is found that the formation height for these lines is in a range from the upper photosphere to the middle chromosphere (e.g., Solanki et al. 1994; Uitenbroek et al. 1994; Clark et al. 1995; Uitenbroek 2000; Ayres 2002; Asensio Ramos et al. 2003; Wedemeyer-Böhm et al. 2005; Stauffer et al. 2022). However, the temperature in the temperature minimum region from the

classical model of solar atmosphere is about 4400 K, based on the emissions of strong Mg II h and k lines and ultraviolet (UV) lines (e.g., Staath & Lemaire 1995; Uitenbroek 1997; Carlsson et al. 1997). This provides a great challenge for us to understand the thermal structures of the lower solar atmosphere.

Early observations of sunspots by Uitenbroek et al. (1994) and Clark et al. (2004) with CO lines revealed the inverse Evershed flow in the penumbra; in other words, the flow moves from the quiet-Sun (QS) region into the umbra. Penn & Schad (2012) found highly sheared flow in the vicinity of sunspots after an X-class flare. Observations of QS and sunspots both show oscillations in CO line center intensity and Doppler velocity, with a period of 3 minutes and 5 minutes, respectively (e.g., Noyes & Hall 1972; Uitenbroek et al. 1994; Solanki et al. 1996; Uitenbroek 2000; Li et al. 2020).

A two-component temperature model has been proposed that contains hot flux tubes and cool nonmagnetic atmospheres;

the latter is named CO-cooled clouds or COmosphere (Ayres 1981; Ayres et al. 1986). However, observations show that the CO line intensity for the QS is very dynamic, presumably driven by the granulation motions and the p-mode oscillations (Uitenbroek et al. 1994; Ayres & Rabin 1996; Uitenbroek 2000). This indicates that no nonmagnetic areas can be constantly as cool as "cool clouds". Instead, cool episodes can be found everywhere in the QS regions (Uitenbroek 2000). The result is reproduced in a 3D numerical simulation of the nonmagnetic lower solar atmosphere with the radiation chemo-hydrodynamics code CO5BOLD (Wedemeyer-Böhm et al. 2006). Recently, the cool low chromospheric gas is also found in a QS region from Atacama Large Millimeter/submillimeter Array (ALMA) observations other than infrared CO lines (Loukitcheva et al. 2019).

In this paper we present the observations of pores, and quiet Sun and network magnetic field regions with CO 4.66 μm lines by the state-of-the-art instrument *Cryogenic Infrared Spectrograph (CYRA)* of the *Goode Solar Telescope (GST)* at Big Bear Solar Observatory (BBSO) (Goode & Cao 2012). We analyze the relationship between CO lines emission and magnetic field. The data from radiation magnetohydrodynamic (MHD) simulation with the *Bifrost* code are also employed in this work. Section 2 presents the observations and data reduction. The radiation MHD simulation is described in Section 3. The results are presented in Section 4. We give our conclusion and discussion in Section 5.

2. Observations and data reduction

CYRA is a novel instrument that probes the rich spectral regime of 1.0–5.0 μm in the infrared (IR), which is the first fully cryogenic spectrograph in any solar observatory. It is designed to study the solar activities in the photosphere to chromosphere by observing the unexplored IR regime (Cao et al. 2010; Cao 2012; Yang et al. 2020). We observed two regions near the disk center that contain several pores and the surrounding network magnetic field regions with CYRA at ~20:12 UT on September 8 and ~19:47 UT on September 11, 2018, respectively. We performed a 75-step raster scan over these two regions with the scanning step of 0.8″. The field of view is about ~68″ × 55″(See Figure 1) and the pixel resolution is about ~0.148″. We used the high-quality calibrated data of CYRA, in which the dark and flat field corrections, removing residual bad pixels and hot pixels, and the non-uniform illumination of spectrum corrections have all been taken into account (Yang et al. 2020).

The data from the *Atmospheric Imaging Assembly* (AIA, Lemen et al. 2012) and the *Helioseismic and Magnetic Imager* (HMI, Scherrer et al. 2012) on board the *Solar Dynamics Observatory* (SDO, Pesnell et al. 2012) are also employed in this research. AIA observes the full-disk Sun in two ultraviolet (UV) and seven extreme-ultraviolet (EUV) passbands. The spatial pixel size is about ~ 0.6″ and the time cadences of the UV and EUV observations are 24 s and 12 s, respectively. Here we only use the AIA 1700 Å images. HMI observes the full-disk photosphere at six wavelength positions across the spectral line of Fe I 6173 Å. HMI provides continuum images, Dopplergrams, line-of-sight (LOS) magnetograms, and vector magnetograms. The time cadences of these data are 45 s, 45 s, 45 s, and 12 minutes, respectively, and the spatial pixel resolution is about ~0.5″. Here we use HMI continuum images, LOS, and vector magnetograms.

3. Radiation MHD simulation

The 3D parallel numerical code *Bifrost* is designed to simulate the stellar atmosphere from the convection zone to the corona (Gudiksen & Nordlund 2005; Gudiksen et al. 2011). The simulation considers various physical and boundary conditions by solving MHD partial differential equations with a Cartesian grid. To solve these MHD equations the sixth-order differential operator, fifth-order interpolation procedures, and a third-order Hyman time-stepping scheme are used in the code (Gudiksen et al. 2011). As a highlight of *Bifrost*, three modules are included to handle the radiative transfer: optically thin radiative transfer, chromospheric radiation approximation, and full radiative transfer computations (Gudiksen et al. 2011).

In this work we employ a 3D MHD numerical simulation model of solar atmosphere for an enhanced network magnetic field region calculated with the *Bifrost* code (en024048_hion, http://sdc.uio.no/search/simulations). This simulation contains ~ 504 × 504 × 496 grid points corresponding to a physical volume of ~ 24 × 24 × 17 Mm^3 extending from the convective zone (about -2.5 Mm) to the corona (about 14.5 Mm). The horizontal grid spacing is ~48 km, while the vertical grid spacing varies from ~19 km to ~119 km. The magnetic field strength in the photosphere is about ~50 G on average. And the distance between two dominant opposite polarity regions is ~8 Mm. Non-equilibrium hydrogen ionization is included in the simulation. The data gives 157 time steps (T=385–541) for the evolution of the atmosphere. For our purpose, we selected one time step (T=385) simulation result and calculated a part of the whole physical volume, ~ 8.62 × 8.14 × 1.7 Mm^3 (see Figure 6). The height is from the convective zone top (about -0.6 Mm) to the middle chromosphere (about 1.1 Mm). The parallel RH code is used to synthesize the CO line profiles (Rybicki & Hummer 1991, 1992; Uitenbroek 2001; Pereira & Uitenbroek 2015).

4. Results

4.1. Results from CYRA observation

Figure 1 shows the pores and surrounding regions on September 8 and 11, 2018, observed at the CO continuum, CO 3-2 R14 line center, HMI continuum, and AIA 1700 Å. The pores observed on September 8 are tiny, with an average diameter of less than ~5″. Only one relatively large pore, with a size of ~10″, was observed on September 11. CO continuum and HMI continuum images seem to be similar. The IR granulations are also recognizable in the CO images, while clearer structures are found in HMI continuum images. The difference is a combined result caused by different wavelengths (IR 4660 nm and optical 617.3 nm) with varying formation heights and under different observing conditions (ground-based and space-borne).

Comparing the CO 3-2 R14 line center intensity maps with AIA 1700 Å images, they all present bright network structures. AIA 1700 Å emission is mainly from the temperature minimum region and photosphere (Lemen et al. 2012), while the CO 3-2 R14 line formation height is from the upper photosphere to lower chromosphere. Similar bright network structures seen in both channels are due to the similar formation height. However, CO 3-2 R14 line center intensity images show some dark patches that are not significant in the AIA 1700 Å images. Since CO molecule lines have a source function close to local thermodynamic equilibrium (LTE) in the formation region, their intensities reveal the temperatures in the formation atmosphere (Ayres & Wiedemann 1989; Uitenbroek 2000). Here, we named
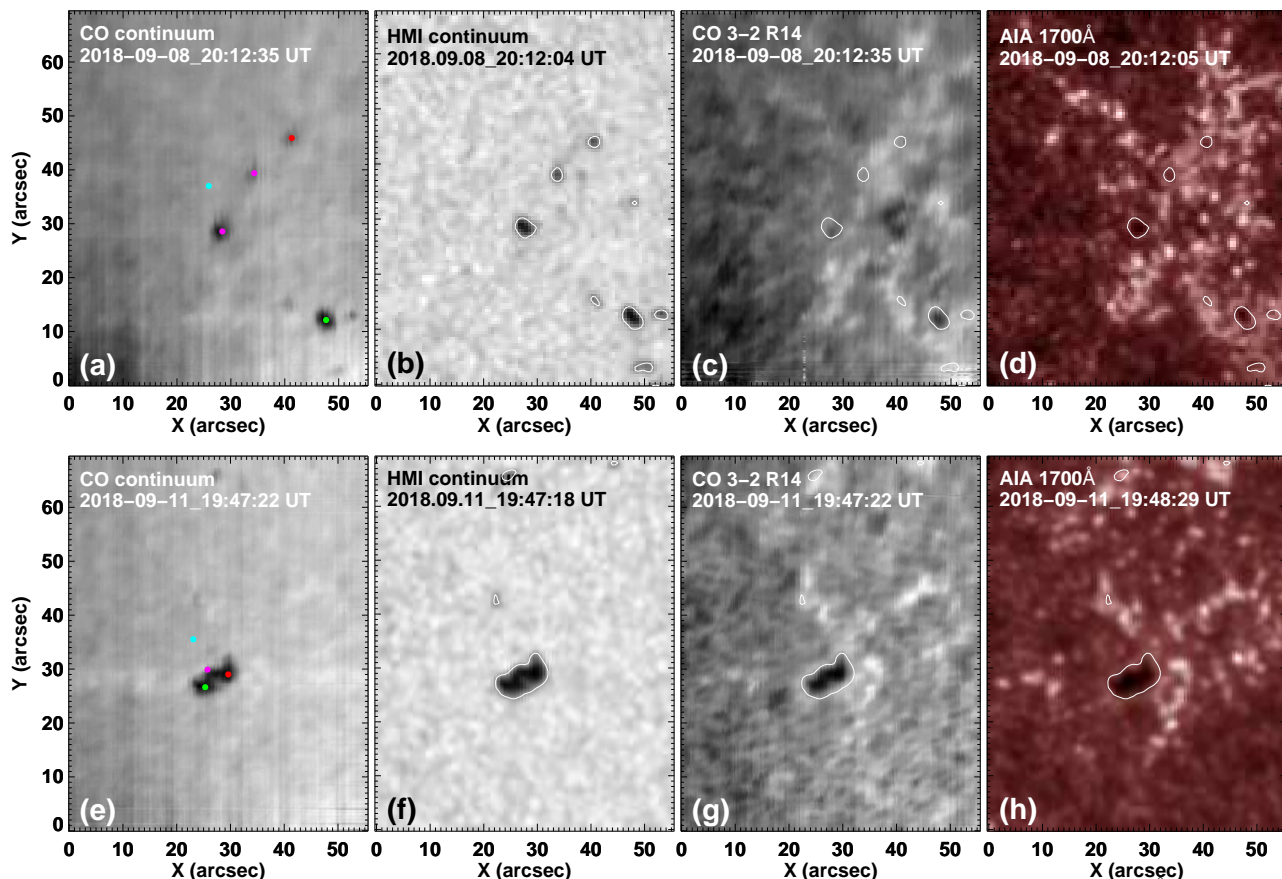
Fig. 1. Overview of pores observed at CO 4.6 μm continuum, HMI continuum, CO 3-2 R14 line center, and AIA 1700 Å. The upper (a-d) and lower (e-h) panels were observed on September 8 and 11, 2018, respectively. The white contours indicate the enhanced absorption features (pores) in HMI continuum intensity images. The colored dots in panels (a) and (e) give the positions of the CO spectral lines shown in Fig. 2(a, b).
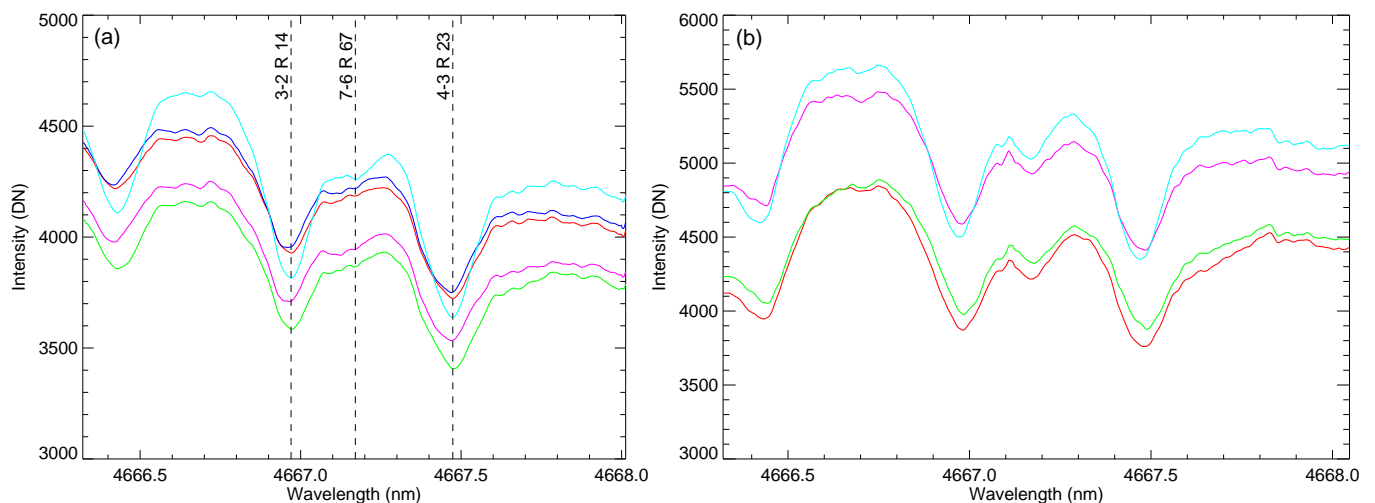

Fig. 2. Plots of CO spectrum around 4.66 μm in different regions. Panels (a) and (b) are for pores and the quiet Sun (cyan) indicated by the colored dots in Fig. 1(a) and (e). The dashed lines in panel (a) indicate three typical CO lines around 4.66 μm. The left panel (a) and right panel (b) are for September 8 and 11, 2018, respectively.

these dark patches "cold bubbles," indicating these regions owing to low-temperature gas or plasma. These cold bubbles are contoured in Figure 3.

We compare the spectral lines near 4.66 μm in the pores and the QS region in Figure 2(a) and 2(b) for the two days, respectively. Four points in the four larger pores are selected for September 8; for September 11 we selected three points in the

pore. The locations of the selected points are indicated by colored dots in Figure 1 (a) and 1(e). The shapes of these spectral profiles of different pores or at different pore positions are similar, but their intensities can be different. This may be caused by different temperatures in the pores, due to different heating effects in differently size magnetic flux tubes (Spruit 1981). The spectral profiles in the QS region (cyan line), on the contrary, are
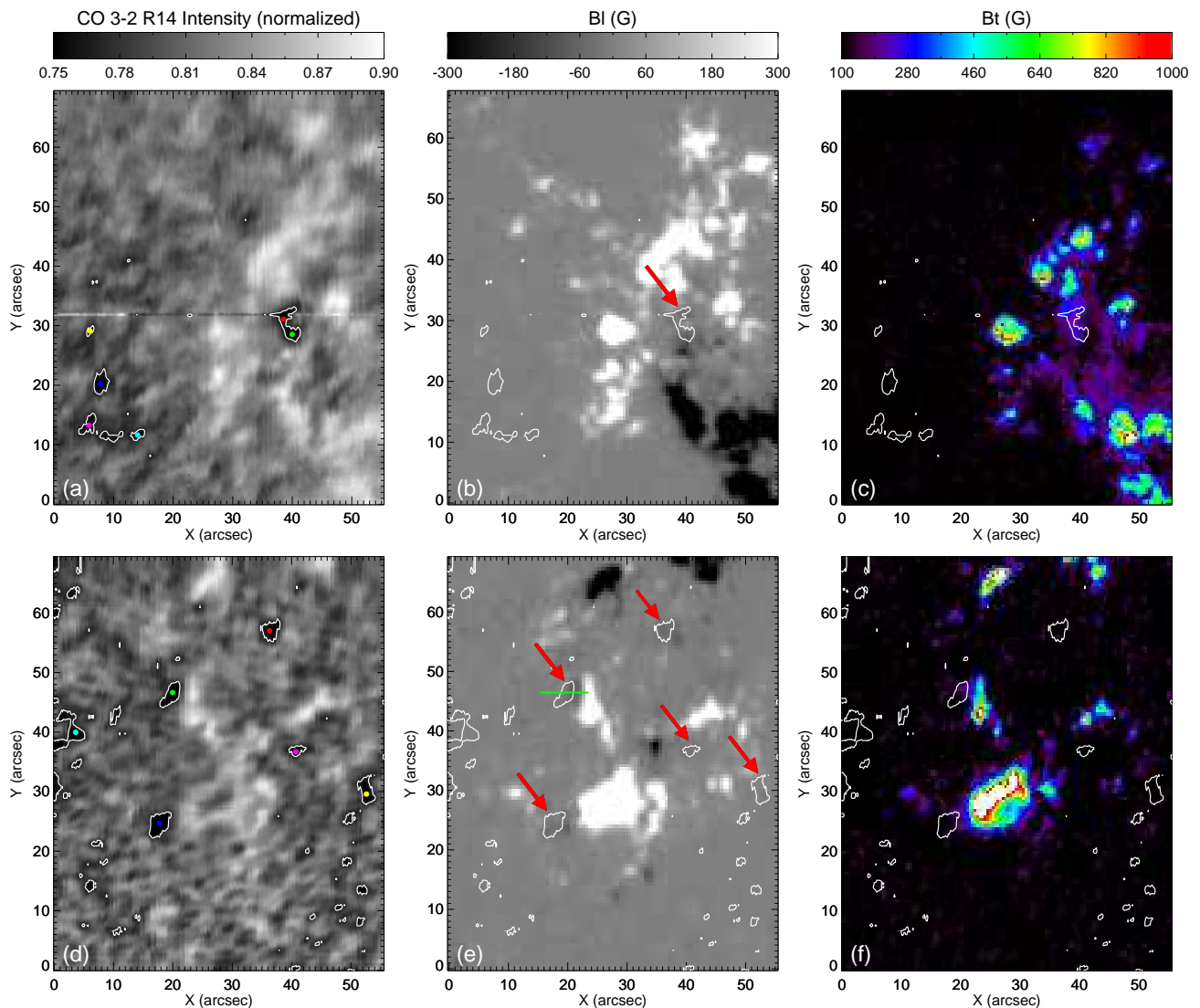
Fig. 3. Normalized CO 3-2 R14 line center intensity images, HMI line-of-sight magnetograms, and horizontal magnetic field. The top (a-c) and bottom (d-f) panels are for September 8 and 11, 2018, respectively. The white contours indicate the dark regions (cold bubbles) in the normalized CO 3-2 R14 line center intensity map with a level of $I_{3-2R14}/I_{continuum} = 0.77$. The red arrows indicate the cold bubbles near or surrounded by magnetic fields. The colored dots in panels (a) and (d) give the positions where we show the normalized CO spectral lines in Fig. 4(a, b). The green line in panel (e) is the slit on which we show the changes of the CO 3-2 R14 line center intensity and B_l strength in Fig. 8 (a).

notably different. Its continuum emission is more significant than that in pores. However, at CO absorption line centers such as 3-2 R14, its emission can be lower than some pores. This should result from different temperature structure models in pores and a QS atmosphere. In particular, the pores are regions with strong magnetic fields, while the quiet Sun is not.

Figure 3 shows images for normalized CO 3-2 R14 line center intensity ($I_{3-2R14}/I_{continuum}$), LOS magnetic field (B_l), and horizontal magnetic field (B_t). We indicate some cold bubbles (dark patches) by white contours with a level of $I_{3-2R14}/I_{continuum} = 0.77$. The shapes are not uniform; the sizes vary from less than $\sim1''$ to about $\sim5''\times6''$. These cold bubbles can be classified into two types according to their locations. One type is located in the QS region without any magnetic fields. The other type is near or surrounded by magnetic fields, as shown by the red arrows in Figure 3(b) and 3(e). The cold bubble indicated by the red arrow in panel (b) observed on September 8 is surrounded by the network magnetic fields. The strength of B_l

in this region is weaker than the surrounding area, but the horizontal magnetic field B_t is stronger, with a strength of about 150~300 G. The cold bubbles in panel (e) indicated by red arrows observed on September 11 are mainly near or on the edge of the magnetic network. The horizontal magnetic field B_t in these regions is weaker than the cold bubble surrounded by the network magnetic field in panel (b). This result suggests that cold bubbles exist with different magnetic field structures, including unipolar, bipolar, or even more complicated structures. In a recent work, Stauffer et al. (2022) also reported the CO cold bubbles observed in the region surrounding a large pore, indicating a potential role of the magnetic field in the formation of these cold bubbles.

Normalized spectral lines ($I/I_{continuum}$) of different cold bubbles (colored dots in Figure 3(a) and 3(d)) are shown in panels (a) and (b) of Figure 4. Most of them are very similar, especially for the cold bubbles observed on September 8 (panel 3(a) and 4(a)). For the observation on September 11, the spectral line at
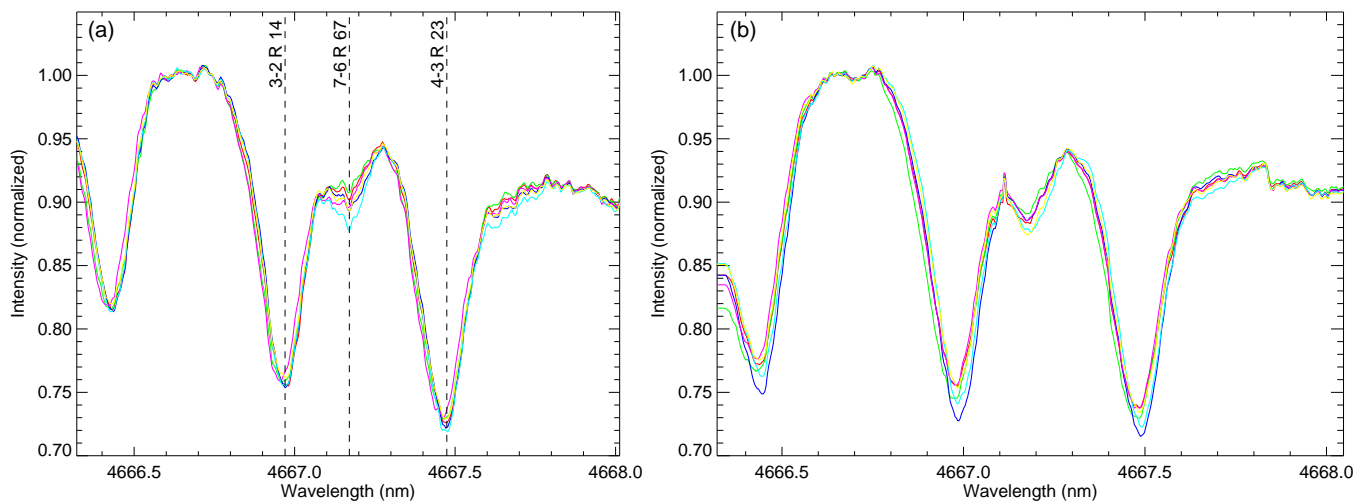
Fig. 4. Normalized ($I/I_{continuum}$) CO spectral lines in cold bubbles indicated by colored dots in Fig.3(a) and (d). The left panel (a) and right panel (b) are for September 8 and 11, 2018, respectively. The dashed lines in panel (a) indicate three typical CO lines around 4.66 μm.
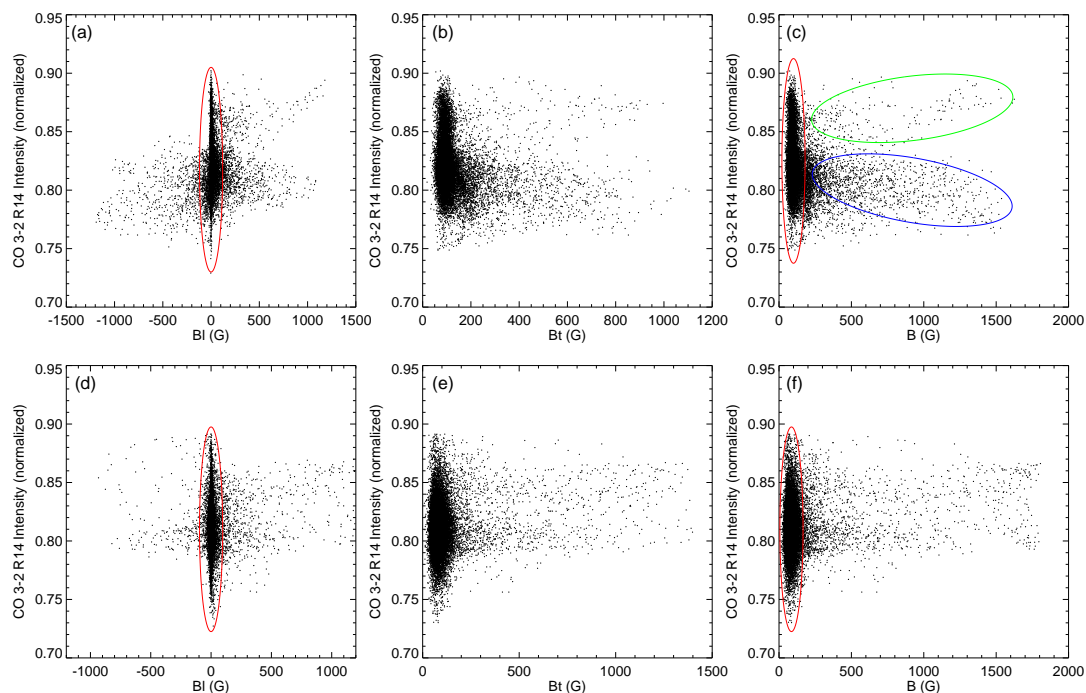

Fig. 5. Scatter plots showing the relationships between the normalized CO 3-2 R14 line center intensity ($I_{3-2R14}/I_{continuum}$) and the line-of-sight magnetic field (B_l), the horizontal magnetic field (B_t), and the total magnetic field strength (B). The top panels (a-c) and bottom panels (d-f) are for September 8 and 11, 2018. The red ellipses indicate the QS regions where the CO 3-2 R14 line center intensity changes in an extensive range. The green ellipse in panel (c) shows that the CO 3-2 R14 line center intensity is brighter when the magnetic field strength is stronger. The blue ellipse reveals the opposite relationship, which means the CO 3-2 R14 line center intensity is inversely proportional to the magnetic field strength.

the position indicated by a blue dot (Fig.3 (d)) in the cold bubble near the pore shows a greater depth in the absorption line center (Fig.4 (b)). The results suggest that most cold bubbles share a similar formation temperature except for specific regions.

Figure 5 shows the scatter plots between normalized CO 3-2 R14 center intensity ($I_{3-2R14}/I_{continuum}$) and the LOS magnetic field B_l, the horizontal magnetic field B_t, and the total magnetic field strength B. The CO 3-2 R14 line intensity in the QS region within the red ellipses changes significantly from the largest absorption depth to the smallest absorption depth, indicating the QS atmosphere is very dynamic. The temperature in this region is not constant as previous studies have shown (e.g., Uitenbroek et al. 1994; Ayres & Rabin 1996; Uitenbroek 2000).

As the magnetic field becomes much stronger, the CO 3-2 R14 line center intensity can be brighter or darker, showing a positive (green ellipse in Fig. 5(c)) or negative correlation (blue
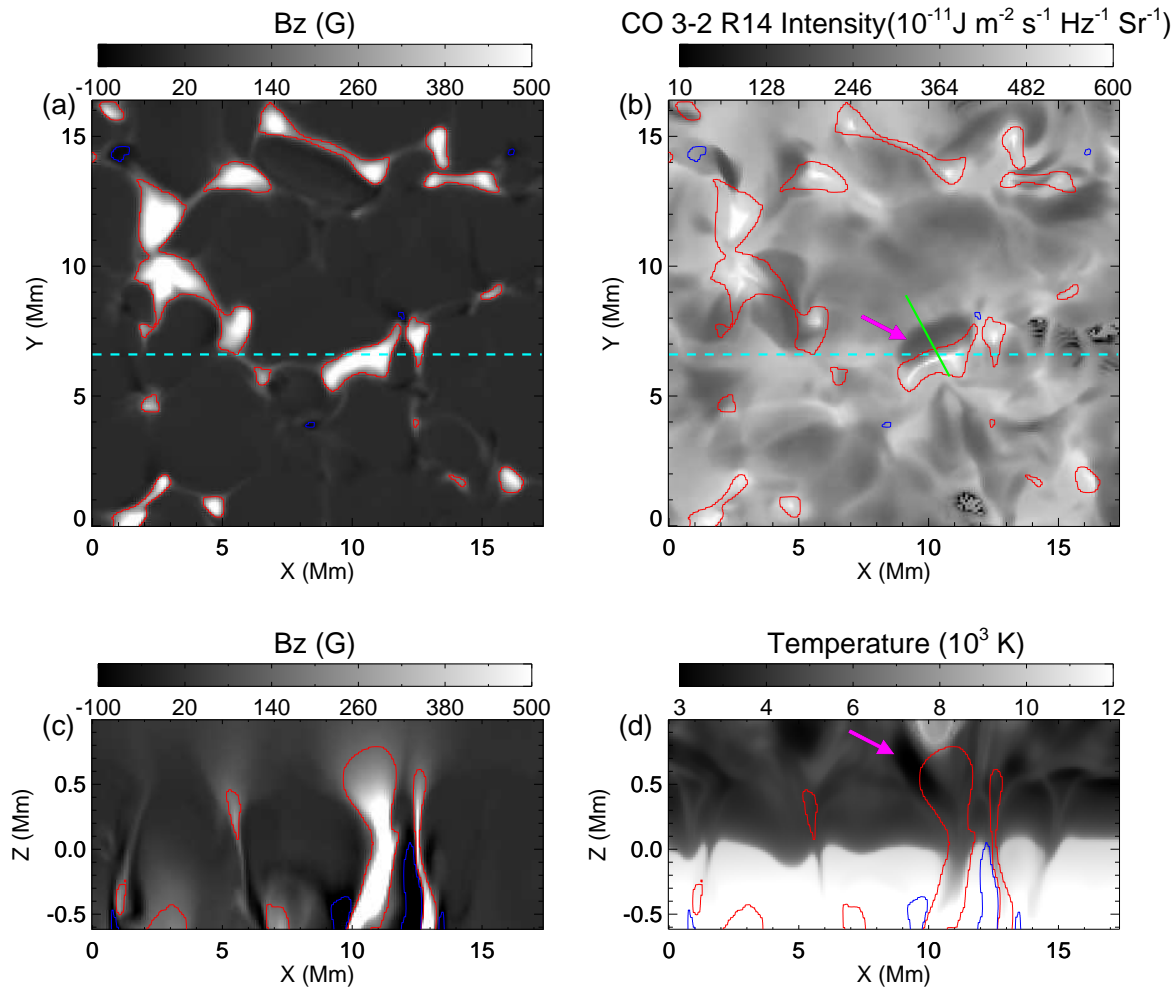
Fig. 6. Radiation MHD simulation results of network magnetic field region with *Bifrost* code. Panels (a) and (b) show the vertical component of the magnetic field (B_z) and synthetic CO 3-2 R14 line center intensity map. Panels (c) and (d) show the strength of B_z and temperature on the slice indicated by the dashed cyan lines in panels (a) and (b). The red and blue contours indicate the positive and negative magnetic fields with 150 G and -50 G, respectively. The magenta arrow in panel (b) indicates a typical cold bubble from the CO 3-2 R14 line center intensity map, which is located near the edge of the magnetic network. Correspondingly, the temperature of the bubble regions at the height of 500 km is lower than the other regions (magenta arrow in panel (d)). The green line in panel (b) indicates the slit showing the relationship of CO 3-2 R14 line center intensity and B_z strength arranged in Fig. 8 (b).

ellipse in Fig. 5(c)). This phenomenon should be caused by different thermal effects on the solar atmosphere for magnetic flux tubes with varying sizes in the formation of pores or network fields (Spruit 1981). However, these two trends are not apparent in the region observed on September 11 (see panel (f)). The possible reason is that only one big pore was observed on September 11, and the strongest magnetic fields are located in the pore (see Figs. 1, 3(e), and 3(f)). Thus, we do not see changes in CO 3-2 R14 line center intensity with different sizes of magnetic flux tubes.

4.2. Results from the Bifrost simulation

There are very few CO 4.6 μm observations at the pore or network magnetic field regions in the past. Moreover, the 3D MHD simulations from Wedemeyer-Böhm et al. (2006) and Uitenbroek (2000) only include the nonmagnetic solar photosphere and low chromosphere and do not have a network mag-

netic solar atmosphere. The state-of-the-art MHD model from the *Bifrost* code contains an enhanced network, giving us an unprecedented opportunity to check whether the synthetic CO emission map under such a condition is consistent with that observed from CYRA.

Figure 6 presents the result of the radiation MHD simulations with *Bifrost* code. Comparing the network magnetic field (Fig. 6(a)) and synthetic CO 3-2 R14 line center intensity map with RH code (Fig. 6(b)), we find a significant part of the cold bubbles with lower line center intensities located on or near the edge of network magnetic field beside the QS areas. The simulation result is consistent with our observations, as shown in Figure 3 and corresponding descriptions. For example, the cold bubble indicated by a magenta arrow in panel (b) is located on the edge of a network magnetic field region. We take cross sections of the vertical magnetic field and temperature for this cold bubble from the position given by the dashed cyan lines in Figure 6(a) and 6(b). The sliced maps are displayed in the bottom panels
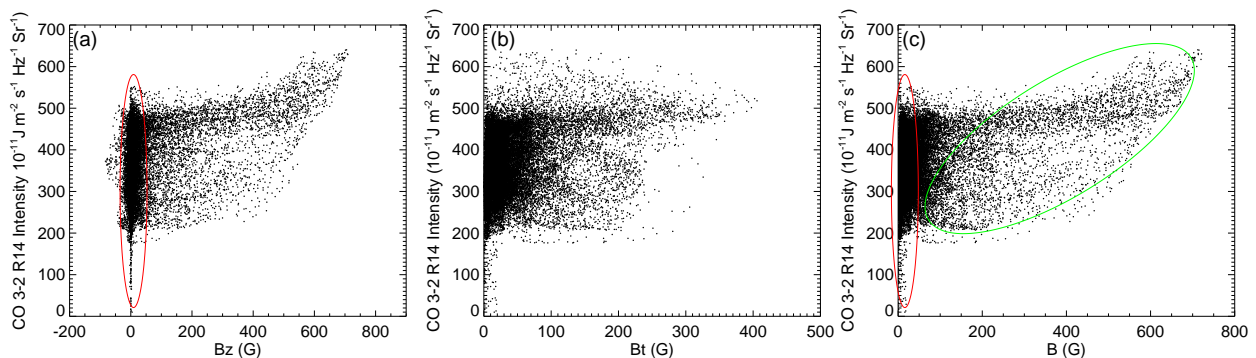
Fig. 7. Similar to Fig.5, but for scatter plots showing the relationships between the CO 3-2 R14 line center intensity and the vertical magnetic field (B_z), the horizontal magnetic field (B_t), and the total magnetic field strength (B) for the *Bifrost* data seen in Fig.6.
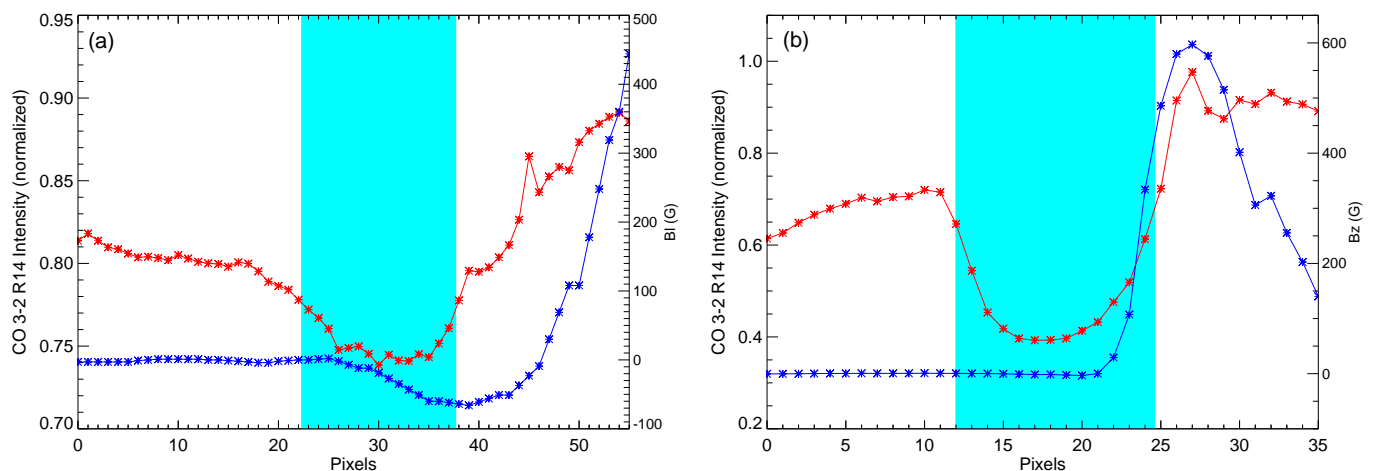

Fig. 8. Normalized CO 3-2 R14 line center intensity (red) and B_l or B_z strength (blue). Panel (a) is along the slit indicated by the green line in Fig. 3(e), and panel (b) is along the slit shown in Fig. 6(b). The cyan shading indicates the edge of the network magnetic field regions.

of Figure 6. The magenta arrow in panel (d) indicates a low-temperature plasma blob. Its temperature is lower than 4000 K, and it is situated in height from ~400 km (upper photosphere) to ~900 km (lower chromosphere), which is in the typical formation height of CO 3-2 R14 line. The "cold plasma blob" located on the edge of the network magnetic field region produced the observed cold bubble in the CO line center map.

Figure 7 presents the scatter plots between the CO 3-2 R14 center intensity and magnetic field B_z, B_t, B_t for the *Bifrost* data. Similarly to Figure 5, we see the CO 3-2 R14 line intensity in the QS region changes within a great range, and the intensity becomes much brighter with the stronger magnetic field. It is also consistent with our observations, as shown in Figure 5 and corresponding descriptions.

Figure 8 exhibits the plots of CO 3-2 R14 line center intensity and magnetic field strength (B_l, B_z) along the slits in Figure 3(e) and Figure 6(b), respectively. Both observation and simulation share a similar change. From the outer part of the magnetic network to the inner part, the CO 3-2 R14 line center intensity first changes to darker, then changes to brighter. The darkest part is located at the edge of the magnetic network. Observations and numerical simulations both show that the cold bubbles can exist in an environment with magnetic fields.

5. Conclusion and discussion

We carried out the observations of pores and surrounding network magnetic field regions in the IR CO 4.66 μm with the new generation and fully cryogenic BBSO/CYRA. To better understand the observations, we also synthesized the CO line center intensity map of a network magnetic field region for the first time with RH code from the *Bifrost*-based 3D radiation MHD model. In the paper, we mainly focus on the relationship between CO lines emission and magnetic field, which was rarely investigated in previous studies (e.g., Ayres 1981; Ayres et al. 1986; Uitenbroek et al. 1994; Ayres 1998; Wedemeyer-Böhm et al. 2006). Supporting the previous studies, significant intensity changes of the CO 3-2 R14 line are observed in the QS region without magnetic fields, indicating the solar atmosphere in this region is highly dynamic in temperature. As the magnetic field gets stronger, we find the CO 3-2 R14 line center intensity will change to be brighter or darker, which results from different thermal effects by flux tubes with different sizes (Spruit 1981).

We also find some cold bubbles from CO 3-2 R14 line center intensity images. They can be classified into two types based on their locations, located in the quiet Sun and near or on the edge of the magnetic network. Our simulation successfully reproduced these two types of cold bubbles. The second type (cold bubbles with magnetic fields) is rarely reported, due to the lim-

ited observations. Our study shows this type should be prevalent from the two days of observations and the simulation.

Two types of cold bubbles indicate different cooling mechanisms in the solar atmosphere. One is without magnetic fields in the quiet Sun, as previous studies show (e.g., Uitenbroek 2000; Wedemeyer-Böhm et al. 2006), and the other includes magnetic fields. The deepest part of the CO 3-2 R14 line center intensity of some cold bubbles corresponds to the edge of the magnetic network (Fig. 8). According to the MHD simulation, the magnetic field can prevent heating from the lower solar atmosphere and form a cold plasma blob. Observations and simulations both illustrate that the magnetic field plays a vital role in the generation and dynamic evolution of some CO cold bubbles.

The question arises of how to understand the mechanism of the magnetic field in producing CO cold bubbles. In early observations, Ayres (1981) reported "thermal shadows" around small sunspots. The author explained that a thermal shadow is formed by the near-surface horizontal magnetic field, which suppresses convection and yields cooler temperature in the upper atmosphere. It is reasonable, although it may need strong and low horizontal magnetic fields. In a recent work by Stauffer et al. (2022), they found several CO cold bubbles that surround a large pore. By calculating the radially averaged three-minute power surrounding the pore in different observational lines, they proposed that the canopy magnetic field prevents the acoustic energy from propagating upward to heat the lower chromosphere. Although there are some differences between the pictures of Ayres (1981) and Stauffer et al. (2022), they both emphasize the important role of the horizontal magnetic field in some cold bubbles. Similarly, cold bubbles near the pore are also recorded in our two days of observations. The very existence of a strong horizontal magnetic field in a region of cold bubbles (Fig.3 (b) and (c)) supports the explanations of both Ayres (1981) and Stauffer et al. (2022).

However, based on our observation and MHD simulation, we also propose another possible mechanism: massive CO molecules generated by cooling and overshooting of granulation adiabatic expansion horizontally accumulate to the boundary of supergranulation. The boundary of supergranulation is where the network magnetic fields is located. Masses of CO molecules can produce radiative cooling and form deep-absorption CO lines (Ayres & Rabin 1996; Uitenbroek 2000; Ayres 2002; Penn 2014). It should be noted that the cold bubbles reported by Ayres (1981) and Stauffer et al. (2022) are mainly near or surround small sunspots or pores. Unprecedentedly, we notice some cold bubbles located near or just on the edge of the magnetic network both from observations and MHD simulations (Figs. 3(e), 3(f) and Figs. 6(b), 6(d)). Particularly, the cold bubbles near the network magnetic field present even stronger absorptions than those inside the network region (Fig.6(b)). The deepest part of CO 3-2 R14 line center intensity corresponds to the edge of the magnetic network (Fig.8).

Our results illustrate the vital role of the magnetic field in the generation of some CO cold bubbles, and highlight the importance of CO observations to better understand the thermal structures of solar atmosphere near the temperature minimum region of different solar features. As CYRA is taking an increasing amount of raster scan data, and the newly constructed Cryogenic Near Infra-Red Spectro-Polarimeter (Cryo-NIRSP) from the Daniel K. Inouye Solar Telescope (DKIST) will begin to perform observations, we are looking forward to analyzing the dynamic evolution of cold bubbles in QS and magnetic field regions. Combing CO observations and the evolutions of 3D MHD simulation having magnetic fields, for example the *Bifrost* and

MURaM codes, we will be able to estimate the role of magnetic fields in their generation and evolution in detail.

References

Asensio Ramos, A., Trujillo Bueno, J., Carlsson, M., & Cernicharo, J. 2003, ApJ, 588, L61
Ayres, T. R. 1981, ApJ, 244, 1064
Ayres, T. R. 1998, in New Eyes to See Inside the Sun and Stars, ed. F.-L. Deubner, J. Christensen-Dalsgaard, & D. Kurtz, Vol. 185, 403
Ayres, T. R. 2002, ApJ, 575, 1104
Ayres, T. R. & Brault, J. W. 1990, ApJ, 363, 705
Ayres, T. R. & Rabin, D. 1996, ApJ, 460, 1042
Ayres, T. R. & Testerman, L. 1981, ApJ, 245, 1124
Ayres, T. R., Testerman, L., & Brault, J. W. 1986, ApJ, 304, 542
Ayres, T. R. & Wiedemann, G. R. 1989, ApJ, 338, 1033
Cao, W. 2012, IAU Special Session, 6, E2.02
Cao, W., Gorceix, N., Coulter, R., et al. 2010, Astronomische Nachrichten, 331, 636
Carlsson, M., Judge, P. G., & Wilhelm, K. 1997, ApJ, 486, L63
Clark, T. A., Lindsey, C., Rabin, D. M., & Livingston, W. C. 1995, in Infrared tools for solar astrophysics: What's next?, ed. J. R. Kuhn & M. J. Penn, 133
Clark, T. A., Plymate, C., Bergman, M. W., & Keller, C. U. 2004, in American Astronomical Society Meeting Abstracts, Vol. 204, American Astronomical Society Meeting Abstracts #204, 37.20
Farmer, C. B. & Norton, R. H. 1989, A high-resolution atlas of the infrared spectrum of the sun and the earth atmosphere from space. A compilation of ATMOS spectra of the region from 650 to 4800 cm^{-1} (2.3 to 16 μm). Vol. II. Stratosphere and mesosphere, 650 to 3350 cm^{-1}.
Goode, P. R. & Cao, W. 2012, in Society of Photo-Optical Instrumentation Engineers (SPIE) Conference Series, Vol. 8444, Ground-based and Airborne Telescopes IV, ed. L. M. Stepp, R. Gilmozzi, & H. J. Hall, 844403
Gudiksen, B. V., Carlsson, M., Hansteen, V. H., et al. 2011, A&A, 531, A154
Gudiksen, B. V. & Nordlund, Å. 2005, ApJ, 618, 1020
Lemen, J. R., Title, A. M., Akin, D. J., et al. 2012, Sol. Phys., 275, 17
Li, D., Yang, X., Bai, X. Y., et al. 2020, A&A, 642, A231
Loukitcheva, M. A., White, S. M., & Solanki, S. K. 2019, ApJ, 877, L26
Noyes, R. W. & Hall, D. N. B. 1972, ApJ, 176, L89
Penn, M. J. 2014, Living Reviews in Solar Physics, 11, 2
Penn, M. J. & Schad, T. 2012, in American Astronomical Society Meeting Abstracts, Vol. 220, American Astronomical Society Meeting Abstracts #220, 206.10
Pereira, T. M. D. & Uitenbroek, H. 2015, A&A, 574, A3
Pesnell, W. D., Thompson, B. J., & Chamberlin, P. C. 2012, Sol. Phys., 275, 3
Rybicki, G. B. & Hummer, D. G. 1991, A&A, 245, 171
Rybicki, G. B. & Hummer, D. G. 1992, A&A, 262, 209
Scherrer, P. H., Schou, J., Bush, R. I., et al. 2012, Sol. Phys., 275, 207
Solanki, S. K., Livingston, W., & Ayres, T. 1994, Science, 263, 64
Solanki, S. K., Livingston, W., Muglach, K., & Wallace, L. 1996, A&A, 315, 303
Spruit, H. C. 1981, in NASA Special Publication, ed. S. Jordan, Vol. 450, 385–413
Staath, E. & Lemaire, P. 1995, A&A, 295, 517
Stauffer, J. R., Reardon, K. P., & Penn, M. 2022, ApJ, 930, 87
Uitenbroek, H. 1997, Sol. Phys., 172, 109
Uitenbroek, H. 2000, ApJ, 531, 571
Uitenbroek, H. 2001, ApJ, 557, 389
Uitenbroek, H., Noyes, R. W., & Rabin, D. 1994, ApJ, 432, L67
Wedemeyer-Böhm, S., Kamp, I., Bruls, J., & Freytag, B. 2005, A&A, 438, 1043
Wedemeyer-Böhm, S., Kamp, I., Freytag, B., Bruls, J., & Steffen, M. 2006, in Astronomical Society of the Pacific Conference Series, Vol. 354, Solar MHD Theory and Observations: A High Spatial Resolution Perspective, ed. J. Leibacher, R. F. Stein, & H. Uitenbroek, 301
Yang, X., Cao, W., Gorceix, N., et al. 2020, in Society of Photo-Optical Instrumentation Engineers (SPIE) Conference Series, Vol. 11447, Society of Photo-Optical Instrumentation Engineers (SPIE) Conference Series, 11447AG